Molecular adsorption on the surface of strongly correlated transition-metal oxides: A case study for CO/NiO(100)

A. Rohrbach, J. Hafner, and G. Kresse
Institut für Materialphysik and Center for Computational Material Science, Universität Wien, Sensengasse 8/12, A-1090 Wien, Austria
(Received 15 April 2003; revised manuscript received 15 October 2003; published 25 February 2004)

It is well known that the physical properties of some transition-metal compounds (mostly oxides) are strongly affected by intra-atomic correlations. Very recently, investigations of the adsorption of small molecules such as CO on the surfaces of transition-metal oxides have led to rather surprising results: the weak adsorbate-substrate bonding and the asymmetric (tilted) adsorption geometries contrast sharply the strong bonding and symmetric geometries characteristic for metallic surfaces. Calculations based on either Hartree-Fock or density-functional methods have failed to explain these observations. For bulk transition-metal oxides it has been demonstrated that the addition of a Hubbard-type on-site Coulomb repulsion U to the local-density Hamiltonian leads to an improved description of the electronic structure of these materials, but a consistent description of all physical properties proved to be elusive. In the present work, we present a comprehensive investigation of bulk NiO and of clean and CO-covered NiO(100) surfaces. We demonstrate that adding the on-site Coulomb repulsion to the spin-polarized gradient-corrected density-functional Hamiltonian leads to a consistently improved description of a wide range of cohesive, electronic, and magnetic properties of NiO (bulk and surface) and a very accurate description of the adsorption properties of CO. The effects of the strong electronic correlations in the substrate on the adsorbate-substrate bonding are discussed in detail.

DOI: 10.1103/PhysRevB.69.075413 PACS number(s): 68.43.Bc, 68.47.Gh, 71.27.+a, 73.20.At

I. INTRODUCTION

The surfaces of metal oxides, and in particular transition-metal oxides, play an extremely important role in heterogeneous catalysis, either as active catalysts or as support for nanostructured metallic catalysts.[1–3] The adsorption and reactions of molecules on metallic surfaces have been studied extensively by both experimental and theoretical techniques. Due to the progress realized in computational density-functional theory (DFT), excellent agreement between theory and experiment has been achieved for the structural parameters characterizing the adsorbate-substrate complex: usually adsorbate-substrate bond lengths can be calculated within a few hundreds of an angstrom, and vibrational frequencies with a maximum error of 3 pct. Energy barriers of surface reactions can be predicted with an accuracy sufficient for a quantitative analysis of reaction rates.[4]

On the other hand, despite the considerable fundamental and industrial interest, our knowledge of transition-metal oxide (TMO) surfaces is much more limited. Experimental data, especially for molecular adsorbates on transition-metal oxides, are rather scarce. This is due to both the difficulties in preparing well-characterized single-crystal surfaces and to the fact that the application of electron emitting or adsorbing spectroscopic techniques to insulating surfaces is difficult due to charging. In theoretical studies, standard density-functional techniques often fail in predicting even the most fundamental properties of bulk transition-metal oxides such as the presence or absence of a gap at the Fermi level; e.g., local-spin-density calculations predict NiO to be either metallic or a semiconductor with a very narrow gap, whereas in experiment[5–9] it is found to be an antiferromagnetic insulator with a gap ranging between 4.0 eV and 4.3 eV. Similar discrepancies between theory and experiment have been encountered for many TMO's. Under these circumstances, only a very few attempts have been made to study molecular reactions on TMO surfaces.

The failure of density-functional theory is due to the fact that the electronic structure of many TMO's is dominated by the strong on-site Coulomb repulsion (strong correlation) between the d electrons. A number of attempts have been made to overcome the limitations of the local-spin-density-approximation (LSDA) for TMO's. Again NiO may serve as a very illustrative example. For NiO these ''beyond-LSDA'' investigations include the GW treatments of Aryasetiawan and Gunnarsson[10] and of Massidda *et al.*,[11] the self-interaction corrections (SIC) to the LSDA of Svane and Gunnarsson[12] and of Szotek *et al.*,[13] the three-particle correction to the LSDA proposed by Calandra and Manghi,[14] the LSDA+U method developed by Anisimov *et al.*,[15] reformulated by Liechtenstein *et al.*[16] and applied to NiO by Dudarev *et al.*,[17] and a Hartree-Fock study by Towler *et al.*[18] Very recently, Bredow and Gerson[19] have applied unrestricted Hartree-Fock, gradient-corrected DFT, and hybrid techniques to investigate the bulk properties of NiO. The results of these studies may be summarized as follows (again these conclusions concern not only NiO, but a wide class of strongly correlated TMO's): Hartree-Fock (HF) calculations grossly overestimate the width of the gap and underestimate the cohesive energies. Adding electronic correlation effects in the form of the functional of Lee, Yang, and Parr[20] (HF-LYP) improves the prediction of the cohesive energy without, however, correcting the band gap. Adding generalized gradient corrections to the LSDA leads to a reasonable cohesive energy and lattice constant, but produces only a minimal gap of 0.4 eV. This can be corrected either by adding many-body terms (GW or SIC), by using a hybrid functional mixing exact exchange with DFT (B3LYP),[21] or by adding a Hubbard term describing the strong on-site Coulomb repul-

sion U to the LSDA Hamiltonian (DFT+U). All three methods lead to the opening of a gap ranging between 2.6 eV (SIC), 3.0 eV (LSDA+U, depending on the strength of the on-site potential U), and 4.2 eV (B3LYP). Qualitatively, there is a general agreement that the top of the valence band is of mixed Ni-d and O-p character, whereas the bottom of the conduction band is Ni-d-like. Hence while the gap is caused by the Ni-d correlation, it is neither of a pure Mott-Hubbard d-d nor of a pure charge-transfer (O-p–Ni-d) type. However, even within the post-DFT approaches differences in quantitative predictions for band gap, exchange splitting, and other physical properties persist.[10–13,17,19]

The electronic structure of TMO surfaces has been studied experimentally using x-ray photoemission spectroscopy (XPS), electron-energy-loss spectroscopy (EELS), and scanning tunneling microscopy (STM). For NiO(100) surfaces, extensive EELS work of Gorschlüter and Merz[22] yields information on surface d-shell excitation. Atomically resolved STM images of the NiO(100) surfaces[23] show the surprising result of a contrast reversal when the applied bias voltage is reversed. Out of the many techniques that have been used to study bulk NiO, only the LSDA+U approach has been applied to extended TMO surfaces. Calculations by Dudarev *et al.*[24] found two types of surface states on NiO(100), a filled state consisting primarily of p_z orbitals on the oxygen atoms and an empty surface state originating from Ni-$d_{3z^2-r^2}$ orbitals. These surface states explain the observed contrast reversal and suggest that at the surface the charge-transfer character of the gap might be more pronounced than in the bulk.

Experimental determinations of the structural properties of molecular adsorbates on TMO surfaces have been performed for the model systems CO, NO, and NH_3 adsorbed on a NiO(100) surface.[25–27] The comparison of the measured bond lengths and adsorption energies of the same species on a metallic Ni surface demonstrated that the adsorption on the surface of the TMO is much weaker than on a metallic surface. In addition, all three adsorbed molecules were found in a tilted configuration instead of in a strictly vertical position like on most metal surfaces. The tilt angle is relatively modest for CO ($12\pm6°$) and NH_3 ($7\pm6°$), but as large as 45° for NO. Quantum-chemical *ab initio* calculations for small NiO clusters on the Hartree-Fock level[28–30] produced significantly larger bond lengths and even lower adsorption energies with respect to experiment and failed to reproduce the observed tilting of the adsorbates. This result was interpreted as a significant ''failure of current theoretical methods.''[26,27] Very recently, Di Valentin *et al.*[31] and Bredow[32] have performed cluster calculations on the adsorption of NO (Ref. 31) and CO (Ref. 32) on NiO(100) using Hartree-Fock, density-functional, and hybrid methods. Both groups of authors come to somewhat different conclusions. Di Valentin *et al.* argue that although bonding of NO to NiO cannot be described by single-determinant approaches (and consequently by DFT), spin-polarized DFT calculations with hybrid functionals lead to reasonable adsorption geometries (including the tilt of the adsorbed molecule). However, a strong dependence on the exchange-correlation functional is noted for the adsorption strength (from strongly bound to unbound) and the spin properties, and this is attributed to different descriptions of the Coulomb repulsion within the 3d shell. Bredow reports a good agreement for the Ni-CO bond length (a possible tilting of the molecule was not considered) with the B3LYP functional, but find the molecule to be almost unbound ($E_{ad}=0.02$ eV). Surprisingly, in spite of the very weak adsorbate-substrate interaction, adsorption leads to a large down-shift of the CO stretching frequency which has not been observed experimentally. Hence many questions remain open.

The aim of the present work is twofold.

(i) We have implemented the DFT+U method in its rotationally invariant form proposed by Liechtenstein *et al.*[16] in a full-potential electronic structure code [the Vienna *ab initio simulation package*[33–37] (VASP)]. In this form the DFT+U Hamiltonian is based on the full all-electron orbitals and densities. This should be considered as a step forward compared to the implementation in codes using muffin-tin orbitals and the atomic-sphere approximation.

(ii) The DFT+U approach implemented in VASP has been used to investigate the physical properties of bulk NiO and of clean NiO(100) surfaces, and to perform a detailed investigation of the adsorption of CO molecules on this surface. The experimentally well-characterized CO/NiO(100) system has been used as a test case for exploring the ability of the DFT+U approach to study molecular adsorption on TMO surfaces. We demonstrate that a semilocal spin-polarized generalized gradient approximation (SGGA) to the LSDA functional, together with the on-site Coulomb repulsion U (resulting in a SGGA+U approach) leads to an improved and consistent description of the cohesive, structural, mechanical, electronic, and magnetic properties of bulk NiO and NiO surfaces. Even more importantly, we demonstrate that the SGGA+U approach allows us to describe the adsorption energy and geometry of CO on NiO(100) in almost perfect agreement with experiment. Our paper is organized as follows: In Sec. II we recapitulate the foundations of the DFT+U approach and its implementation in VASP within the framework of the projector-augmented wave (PAW) method.[38,37,39] Sections III and IV describe the results for bulk NiO and a clean NiO(100) surface, demonstrating that a SGGA+U approach leads to an accurate and consistent description of bulk and surface properties. Section V presents a detailed study of the adsorption properties of CO on NiO(100) in the LSDA, SGGA, LSDA+U, and SGGA+U approximations, and we conclude in Sec. VI.

II. THEORETICAL METHODS

A. DFT+U method

Transition-metal compounds such as NiO experience a strong on-site Coulomb-repulsion amongst Ni-3d electrons due to the narrow d-band-width, which is not correctly described in a spin-polarized DFT treatment. This error can be corrected with the DFT+U method, which is a combination of the DFT in either the LSDA or SGGA and a Hubbard Hamiltonian for the Coulomb repulsion and exchange interaction. For the present calculations we use a simple DFT

$+U$ version, proposed by Dudarev *et al.* in Ref. 17. It is based on a model Hamiltonian with the form[17]

$$\hat{H}=\frac{U}{2}\sum_{m,m',\sigma}\hat{n}_{m,\sigma}\hat{n}_{m',-\sigma}+\frac{(U-J)}{2}\sum_{m\neq m',\sigma}\hat{n}_{m,\sigma}\hat{n}_{m',\sigma}, \tag{1}$$

where $\hat{n}_{m\sigma}$ is the operator yielding the number of electrons occupying an orbital with magnetic quantum number m and spin σ at a particular site.

The Coulomb repulsion is characterized by a spherically averaged Hubbard parameter U describing the energy increase for placing an extra electron on a particular site, $U=E(d^{n+1})+E(d^{n-1})-2E(d^n)$, and a parameter J representing the screened exchange energy. While U depends on the spatial extension of the wave functions and on screening, J is an approximation to the Stoner exchange parameter and almost constant ~ 1 eV. The Mott-Hubbard Hamiltonian includes energy contributions already accounted for by the DFT functional. To correct for this ''double counting,'' Eq. (1) is estimated in the limit of integer occupancies and subtracted from the DFT energy to obtain the spin-polarized DFT$+U$ energy functional.[24,17] A simple functional is obtained after some straightforward algebra:[17]

$$E_{DFT+U}=E_{DFT}+\frac{U-J}{2}\sum_{m\sigma}(n_{m\sigma}-n_{m\sigma}^2). \tag{2}$$

This energy functional is yet not invariant with respect to a unitary transformation of the orbitals. A formulation given by Liechtenstein *et al.*[16] replaces the number operator by the on-site density matrix ρ_{ij}^{σ} of the d electrons to obtain a rotationally invariant energy functional. In the present case this yields the functional[17]

$$E_{DFT+U}=E_{DFT}+\frac{U-J}{2}\sum_{\sigma}\mathrm{Tr}[\rho^{\sigma}-\rho^{\sigma}\rho^{\sigma}]. \tag{3}$$

The interpretation of this DFT$+U$ functional is particularly simple. In the limit of an idempotent on-site occupancy matrix ρ^{σ},

$$\rho^{\sigma 2}=\rho^{\sigma},$$

the DFT$+U$ functional yields exactly the same energy as the DFT functional $E_{DFT+U}=E_{DFT}$. The second term in Eq. (3) enforces this idempotency. If $U>J$, the term is positive definite, since the eigenvalues ν_i of the on-site occupancy matrix can vary only between 0 and 1:

$$\rho^{\sigma}-\rho^{\sigma}\rho^{\sigma}=\sum_i \nu_i^{\sigma}-\nu_i^{\sigma 2}>0,$$

where the sum on the right-hand side is over all eigenvalues ν_i of the on-site occupancy matrix ρ^{σ}. Hence the second term in Eq. (3) can be interpreted as a positive-definite penalty function driving the on-site occupancy matrices towards idempotency. The DFT$+U$ energy obtained in this manner is always larger than the DFT energy. The ''strength'' of the penalty function is parametrized by a *single* parameter $U-J$. A larger $U-J$ forces a stricter observance of the on-site idempotency. This is achieved by lowering the one-electron potential locally for a particular metal d orbital and in turn modifying the hybridization with the ligand atoms. The one-electron potential is given by the functional derivative of the total energy with respect to the electron density, i.e., in a matrix representation,

$$V_{ij}^{\sigma}=\frac{\delta E_{DFT+U}}{\delta\rho_{ij}^{\sigma}}=\frac{\delta E_{DFT}}{\delta\rho_{ij}^{\sigma}}+(U-J)\left[\frac{1}{2}\delta_{ij}-\rho_{ij}^{\sigma}\right]. \tag{4}$$

It is recognized that filled d orbitals which are localized on one particular site are moved to lower energies, by $-(U-J)1/2$, whereas empty d orbitals are raised to higher energies by $(U-J)1/2$.

B. Implementation within the projector-augmented wave method

The DFT$+U$ is implemented in the PAW method as described by Bengone *et al.*[39] In the PAW method, the all-electron (AE) wave function Ψ_n is related to the pseudo-wave-function $\tilde{\Psi}_n$ through a linear transformation,[38,37]

$$|\Psi_n\rangle=|\tilde{\Psi}_n\rangle+\sum_i(|\phi_i\rangle-|\tilde{\phi}_i\rangle)\langle\tilde{p}_i|\tilde{\Psi}_n\rangle. \tag{5}$$

The index i is a shorthand for the atomic site $\mathbf{R}$, the angular momentum numbers $L=l,m$ and an additional index n referring to the reference energy ϵ_{nl} of the partial waves ϕ_i. The all-electron partial waves ϕ_i are solutions of the Schrödinger equation for a spherical symmetric reference atom, and the pseudo-partial-waves $\tilde{\phi}_i$ are equivalent to the AE partial waves outside a core radius r_c and match continuously onto $\tilde{\phi}_i$ inside the core radius. The projector functions $\tilde{p}_i$ are dual to the partial waves:

$$\langle\tilde{p}_i|\tilde{\phi}_j\rangle=\delta_{ij}.$$

Starting from Eq. (5) it is possible to show that the AE charge density is given by a sum of three terms in the PAW method (for details we refer to Refs. 38 and 37):

$$n(\mathbf{r})=\tilde{n}(\mathbf{r})+n^1(\mathbf{r})-\tilde{n}^1(\mathbf{r}). \tag{6}$$

Here, $\tilde{n}$ is the soft pseudo-charge-density related directly to the pseudo-wave-functions $\tilde{\Psi}_n$. The on-site charge densities $n^1(\mathbf{r})$ and $\tilde{n}^1(\mathbf{r})$ are only defined inside spheres with radius r_c centered around each atom (PAW spheres). For the densities $n^1(\mathbf{r})$ and $\tilde{n}^1(\mathbf{r})$ the following defining equations are obtained:

$$n^1(\mathbf{r})=\sum_{(i,j)}\rho_{ij}^{\mathrm{PAW}}\langle\phi_i|\mathbf{r}\rangle\langle\mathbf{r}|\phi_j\rangle \tag{7}$$

and

$$\tilde{n}^1(\mathbf{r})=\sum_{(i,j)}\rho_{ij}^{\mathrm{PAW}}\langle\tilde{\phi}_i|\mathbf{r}\rangle\langle\mathbf{r}|\tilde{\phi}_j\rangle. \tag{8}$$

The matrix ρ_{ij}^{PAW} describes the occupancies of each augmentation channel (i,j), and is calculated by multiplication of the pseudo-density-operator with the projector functions from the left and right:

$$\rho_{ij}^{\mathrm{PAW}}=\sum_n f_n\langle\tilde{p}_j|\tilde{\Psi}_n\rangle\langle\tilde{\Psi}_n|\tilde{p}_i\rangle. \tag{9}$$

For a complete set of partial waves, the density $n^1(\mathbf{r})$ is exactly equivalent to the exact all electron charge density within the PAW sphere:

$$n(\mathbf{r})=n^1(\mathbf{r}),$$

which is the crucial relation on which the present implementation of the DFT+U method rests.

To derive the PAW+U method, one needs to define the orbital density matrix $\rho_{mm'}$ entering Eq. (3). The natural definition is based on the AE charge density inside the PAW augmentation spheres, $n^1(\mathbf{r})$, which can be written more explicitly as

$$n^1(\mathbf{r})=\sum_{(lmn),(l'm'n')}\rho_{(lmn),(l'm'n')}^{\mathrm{PAW}}\langle\phi_{lmn}|\mathbf{r}\rangle\langle\mathbf{r}|\phi_{l'm'n'}\rangle.$$

With the restriction to l and $l'=2$, one can therefore relate the on-site density matrix $\rho_{mm'}$ to the PAW on-site occupancy matrix $\rho_{(lmn),(lm'n')}^{\mathrm{PAW}}$ through

$$\rho_{mm'}=\sum_{nn'}\rho_{(lmn),(lm'n')}^{\mathrm{PAW}}\langle\phi_{lmn}|\phi_{l'm'n'}\rangle.$$

This establishes the crucial link between the PAW and the DFT+U method. For further details the reader is referred to Ref. 39. At this point we only add a few remarks concerning the implementation of the DFT+U approach in the PAW method in relation to that in other band-structure codes.

(i) Within the PAW method the calculation of the density matrix is based on the extended AE orbitals, whereas, e.g., within the LMTO-ASA (atomic sphere approximation) method it is based on the muffin-tin orbitals defined within overlapping atomic spheres producing only pseudo electron densities.

(ii) The PAW approach is a frozen-core method. A relaxation of the core could influence the results, although we expect this to be less important for NiO than for materials with ''semicore'' states not too far below the bottom of the valence band.

C. Further computational details

In this work, the calculations were performed with VASP.[33–37] VASP is a first-principles plane-wave code, treating exchange and correlation in the DFT scheme. The projector-augmented wave (PAW) method[38] in the implementation of Kresse and Joubert[37] is used to describe the electron-ion interaction. At the level of the LSDA, the exchange-correlation functional proposed by Perdew and Zunger[40] (based on the quantum Monte Carlo calculations of Ceperley and Alder[41]) is used. Generalized gradient corrections (GGC's) are added in the form of the Perdew-Wang[42] functional. For spin-polarized calculations, the spin interpolation of Vosko *et al.*[43] was used. GGC's add, through the dependence of the functional on the gradient of the electron and spin densities, a semilocal element to the purely local LSDA functional. The influence of the GGC's on the results of the calculations of physical properties is by now well documented (see, e.g., Moroni *et al.*[44] and further references given therein).

(i) They correct the overbinding tendency characteristic for the LSDA, leading to smaller cohesive energies and larger equilibrium lattice constants.

(ii) For magnetic systems, GGC's predict a slightly enhanced exchange splitting and larger magnetic moments. Generally, the magnetic state is stabilized relative to the nonmagnetic state—the most striking example is Fe where only the SGGA predicts the correct ground state (body-centered cubic and ferromagnetic), whereas the LSDA predicts nonmagnetic hexagonal Fe to be lower in energy.[44]

(iii) For molecular adsorption at metallic surfaces, the LSDA predicts in many cases a qualitatively incorrect potential-energy surface, whereas the SGGA results in a correct description of the adsorption/desorption dynamics.[45,46]

(iv) The influence of the gradient corrections is largest for the light elements where the overbinding tendency of the LSDA is most severe. For very heavy elements, the GGC's eventually overcorrect the LSDA error. Part of the present study is also aimed at exploring the interplay of the GGC's to the LSDA Hamiltonian with the Hubbard term. This question has hardly received any attention so far.

The Kohn-Sham equations are solved via iterative matrix diagonalization based on the minimization of the norm of the residual vector to each eigenstate and optimized charge- and spin-mixing routines.[47–49] To sample the band structure, the Brillouin-zone integration is performed using Monkhorst-Pack grids.[50] The unit cells are usually extended in one direction due to symmetry breaking in antiferromagnetic setups. k- point grids varying from $3\times3\times1$ to $6\times6\times4$ were used. The densities of states (DOS's) were calculated using the linear tetrahedron method.[51–53] For the calculation of the total energy as a function of volume, a Gaussian-smearing approach with $\sigma=0.2$ eV was used. The plane-wave cutoff was fixed to 330 eV. The DFT+U version of Dudarev *et al.*[17] described above was used for all calculations. Since the DFT+U functional depends only on the difference $U-J$, J was kept fixed to 1 eV during all calculations. The $U-J=0$ case represents the DFT limit.

III. BULK NICKEL OXIDE

Bulk nickel oxide is an antiferromagnetic insulator with an experimental band gap between 4.0 and 4.3 eV according to different experiments.[5–8] It crystallizes in the rocksalt structure with a lattice constant of $a=4.17$ Å. Below its Néel temperature of $T_N=523$ K, it assumes an antiferromagnetic type-II ordering [planes with collinear spins are parallel to the (111) plane] with local magnetic moments of $(1.64–1.77)\mu_B$ at saturation.

A. Influence of strong electronic correlations on physical properties

Calculations of the physical properties of bulk NiO were performed using the LSDA, SGGA, LSDA+U, and SGGA

TABLE I. Band gap $\Delta\epsilon$, lattice constant a, magnetic moment on Ni atoms, m, bulk modulus B, and cohesive energy E with respect to Ni and O_2.

	Experiment	Theory							
		Present work				Dudarev *et al.*[a]		Bredow[b]	
		LSDA+U $U=6.3$ eV	SGGA+U $U=6.3$ eV	SGGA	LSDA	LSDA+U $U=6.3$ eV	LSDA	SGGA	B3LYP
$\Delta\epsilon$ (eV)	4.2,[c] 3.8[d]	3.1	3.2	0.5	0	3.0	0.6	0.4	4.2
a (Å)	4.17[c]	4.07	4.20	4.19	4.07	4.19	4.08	4.18	4.23
m (μ_B)	1.64,[e] 1.77[f]	1.64	1.72	1.28	1.13			1.33	1.68
B (GPa)	205[c]	236	202.5	210	252	182	230		
E (eV)		5.89	−5.03	−5.84	−6.75				

[a]Reference 17.
[b]Reference 19.
[c]Reference 5.
[d]Reference 3.
[e]Reference 7.
[f]Reference 6.

+U. The results are compiled in Table I. We first note that the LSDA yields a 9% too small lattice constant of 4.07 Å, a too large bulk modulus, a 20% too small magnetic moment, and no gap. The SGGA improves the results somewhat by correcting the overbinding characteristic for the LSDA (we also note good agreement with the SGGA results of Bredow and Gerson[19]). A small band gap of 0.5 eV opens, and the local magnetic moment increases to $1.28\mu_B$, both are too small compared to experiment. The lattice constant and the bulk modulus on the other hand agree reasonably well with experiment. There is definitely a need for further improvement by including correlation effects.

To determine the optimal value for the on-site Coulomb potential, U was varied between $U=0$ and $U=9$ eV. Figure 1 shows the dependence of the equilibrium lattice constant, the magnetic moment, and the band gap as calculated in the SGGA+U approach. The lattice parameter shows only a weak dependence on U, while the magnetic moment and the band gap increase monotonously with increasing U. For the magnetic-moment agreement with experiment is achieved at $U\sim 5$ eV, while the measured band gap can be matched only at $U\geqslant 8$ eV. The variation of all physical quantities with U in a LSDA+U approach is similar, but as disagreement between theory and experiment is much larger in the LSDA than in the SGGA, a much larger value of U is required to fit the experimental values (for the lattice constant agreement cannot be achieved for any acceptable value of U) and the scatter of the values required to fit different physical quantities is also much larger. Within the SGGA+U, a value of $U-J=5.3$ eV leads to reasonable values for all considered physical properties: magnetic moment and bulk modulus agree within experimental uncertainty, the lattice constant is $\sim 0.5\%$ too large, although the band gap is still underestimated by nearly 1 eV. To fit the band gap, a value of $U\geqslant 8$ eV is required, such a large value, however, would lead to a bad overall description of the electronic spectrum. We also note reasonable agreement with the results based on the B3LYP hybrid functional.

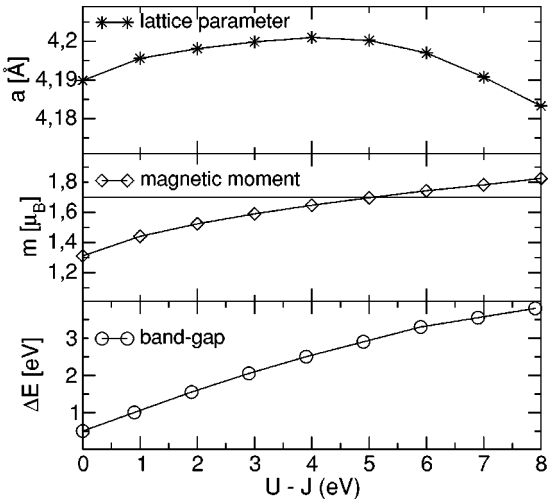

FIG. 1. SGGA+U predictions of lattice constant, magnetic moment, and band gap of bulk NiO plotted against $U-J$.

In the present calculations, the lattice constant is hardly affected by the inclusion of the on-site Hubbard term, in contrast to previous studies using the LMTO-ASA method with similar DFT+U corrections done by Dudarev *et al.*[17] The reason for this discrepancy is not quite clear, but could be due to the frozen-core approximation applied in the present work. As in other DFT+U calculations, the minority e_g orbital is shifted to higher energies by the on-site Coulomb repulsion. This reduces the hybridization between the minority Ni-e_g and O-p orbitals, decreasing the covalent bonding between O-p and e_g states. This process should yield an increase in the volume. In our calculations, however, this seems to be counterbalanced by a contraction of the t_{2g} orbitals which reduces the Pauli repulsion between d orbitals and O-p states.

B. Electronic structure

Figure 2 shows the spin-polarized local density of states on the Ni and O sites as calculated in the SGGA and in the

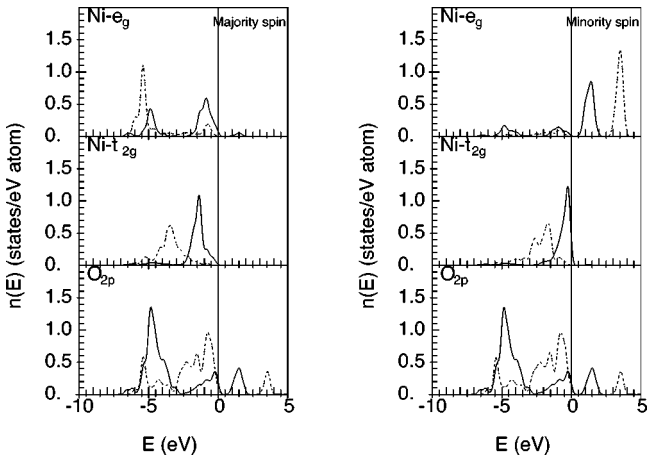

FIG. 2. Projected density of states of bulk Ni-3d and O-2p states from GGA (solid line) and GGA+U, $U=6.3$ eV (dashed line). Energies are given relative to the top of the valence band.

SGGA+U (with $U=6.3$ eV). In the SGGA, the lower part of the valence band is dominated by O-2p states weakly hybridized with the Ni-3d states, the upper part of the valence band and the lowest conduction band are of almost pure Ni-3d character, the top of the valence has Ni-e_g character for the majority spins, and Ni-t_{2g} character for the minority spins. The lowest excited states are minority Ni-e_g states. Hence the small gap that exists in the SGGA is of Mott-Hubbard-type. The SGGA band structure is quite similar to the LSDA result of Bengone *et al.*,[39] but in the SGGA we note a stronger overlap of the t_{2g} and e_g manifolds of the majority states due to a down-shift of the occupied e_g states caused by the larger magnetic moment and exchange splitting than in the LSDA. At increasing U, the exchange splitting of the e_g states is strongly increased, at $U=6.3$ eV we find a value of about 9.5 eV, in good agreement with the GW calculations of Massida *et al.*[11] who report a splitting of 9 eV. The LSDA+U calculations of Bengone *et al.*[39] produce a smaller splitting of 8.6 eV at $U=5$ eV, in accordance with the difference we have already noted between the LSDA and SGGA results. Compared to the O-2p states, the Ni-t_{2g} states are shifted to larger binding energies, resulting in a strongly increased O-2p–Ni-3d hybridization. At the top of the valence band we now have states with predominantly O-2p character and a small admixture of Ni-t_{2g} states for both majority and minority electrons; hence the band gap is a mixture of a charge transfer and a Mott-Hubbard d-d type. At $U=6.3$ eV, the calculated width of the gap is 3.1 eV in the LSDA+U and 3.2 eV in the SGGA+U approximation, in reasonable agreement with the GW gap of 3.5 eV. The SIC calculations of Szotek *et al.*[13] and of Svane and Gunnarsson[12] agree on a smaller gap of 2.5 eV, they also produce a magnetic moment of only $1.5\mu_B$. The mixed Ni-d–O-p character of the top of the valence band is also in good agreement with the B3LYP calculations,[19] although they result in a somewhat broader gap. Increasing the on-site Coulomb repulsion beyond $U\sim 6$ eV leads to an exchange splitting significantly larger than that obtained in the GW calculations and enhances the O-p character of the top of the valence band. The mixed character of the top of the valence band is also confirmed by a comparison of the experimental XPS (Ref. 54) and the O $K\alpha$ x-ray emission spectra.[55,56] The XPS spectrum is dominated by emission from Ni states and the O $K\alpha$ XES spectrum by emission from O-2p states, both spectra show considerable intensity at the top of the valence band.

Detailed investigations of the dispersion of the occupied electronic eigenstates have been performed using angular-resolved ultraviolet photoemission spectroscopy (ARUPS).[25,57] Comparison of theory and experiment at an absolute energy scale is difficult because the experiments have been performed on samples in which the Fermi level was pinned at different energies in the gap. In previous attempts to compare theory and experiments,[39,57] the alignment of the various sets of experimental data and of the theoretical bands has been arbitrarily chosen in order to make experiment and theory agree at the highest valence band at the Γ point. We consider this procedure as quite problematic as it misaligns the spectra with respect to the Fermi level. We proceed in a slightly different way. Figure 3 shows our SGGA and SGGA+U results for the bands along the Γ-X direction, compared with the ARUPS experiments of Shen *et al.*[57] and Kuhlenbeck *et al.*[25] For each data set, the top of the valence band was located at $\Delta\epsilon/2$ below the energy zero at the Fermi level, using the experimental and calculated value of the band gap $\Delta\epsilon$ as appropriate for each case. The ARUPS data show essentially four significant features: the two almost dispersionless features at energies of ~ -2 eV and ~ -3.6 eV marked by triangles in Figs. 3(a) and 3(b) have been assigned, on the basis of the variation of the intensity with the energy of the incident photons, to the Ni-3d band. For these features we note a very good agreement with our SGGA+U calculations. As discussed by Shen *et al.*, the details of the photoemission intensities also show indications for a splitting into several weakly dispersing bands, also in agreement with the calculations. The strongly dispersive features marked by circles in Figs. 3(a) and 3(b) have been assigned to oxygen bands. For the upper of these two bands we find again good agreement with the SGGA+U results. The lower of these two bands shows strong dispersion in the center of the Brillouin zone and is rather flat towards the X point. In this region we note good agreement with the SGGA+U result, whereas the strongly dispersive part cannot be associated with a single continuous band. In both sets of experimental data, an additional feature (not shown in the dispersion relations with a rather weak dispersion) is located at -9 eV binding energy. Its intensity increases strongly with increasing photon energy, which is consistent with its Ni-3d character. This feature agrees quite well with the lower edge of the Ni valence band that is pushed to lower energies by the on-site Coulomb interactions in the SGGA+U—in contrast in a SGGA calculation the lower edge of the band is of oxygen character. The data of Kuhlenbeck *et al.* [see Fig. 3(d)] agree quite well with those of Shen *et al.* Only the lowest Ni band has not been included in this study. Altogether we note a quite satisfying agreement of the SGGA+U results with experiment.

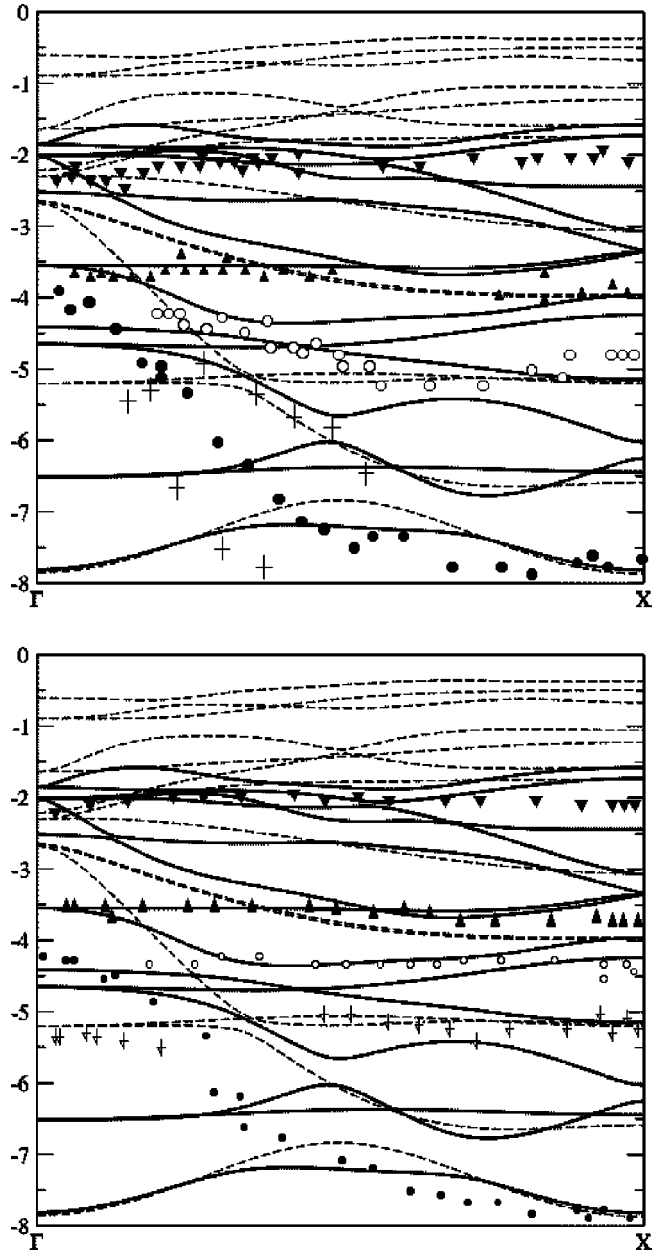

FIG. 3. Dispersion relations of electronic eigenstates in NiO, as calculated using the SGGA (broken lines) and the SGGA+U (full lines) and compared to experiment. The triangles, circles, and crosses represent peaks in the photoemission intensities. The figures show data from Shen *et al.* (Ref. 57), taken at incident angles of (a) 90° and (b) 70° of the photons. For each set of data, the energy scale has been adjusted such as to achieve reasonable agreement for the highest valence band (cf. text).

IV. CLEAN (100) SURFACE

Cleavage of NiO along the (100) plane yields a nonpolar and rather stable surface. The magnetic ordering in the surface plane is antiferromagnetic with parallel spins aligned in nearest-neighbor rows.[59] Table II compares our present results with other theoretical calculations and experiment. The LSDA calculations predict an outward relaxation of the top layer, contrasting the inward relaxation found in the experiment,[58] and a quite substantial buckling of 0.1 Å (the Ni atoms move outwards compared to the O atoms) which has not been observed. The SGGA, LSDA+U, and SGGA +U calculations on the other hand predict a small ($\sim$1%) inward relaxation of the top layer, an even weaker outward relaxation of the subsurface layer, and almost no buckling. The magnetic moment of the Ni surface atoms is almost unaffected by this modest structural relaxation, but the gap is slightly narrowed compared to the bulk. A previous investigation of the NiO surface using LSDA by Dudarev *et al.*[24] has been performed on a bulk-terminated surface geometry, without allowing any relaxation. In accordance to our results, no change in the magnetic moment and a slight band narrowing compared to the bulk have been reported.

The layer-resolved density of states as calculated using SGGA and SGGA+U is shown in Fig. 4.

We first note that the empty minority e_g band splits into two well-separated subbands at the surface. As discussed in Ref. 24, the peak at the conduction band edge originates from the d_{z^2} states which, at the surface, experience only the field originating from the oxygen atoms below the Ni surface atom, whereas the crystal field felt by the $d_{x^2-y^2}$ orbital is hardly modified compared to the bulk. This leads to a sizable reduction of the band gap at the surface from 0.5 eV to 0.1 eV and 3.2 to 2.9 eV in SGGA and SGGA+U respectively. Figure 5 shows the dispersion relations of the electronic eigenstates of our slab model, together with the bulk dispersion relations projected onto the surface Brillouin zone. It is evident that the Ni-e_g surface states are split from the lower edge of the conduction band, whereas at the top of the valence band, all bands merge with the continuum of bulk states. In a scanning tunneling microscopy with positive sample bias, states at the lower conduction-band edge are imaged; the strong localization of the Ni-e_g surface states leads to a rather sharp image contrast.[23,59] Experiments with a negative sample bias on the other hand image states at the top of the valence band. The dominant O-p character of these states explains the contrast reversal observed in the STM experiments as the bias is reversed, the overlap of these states with the bulk bands leads to a significantly more diffuse STM image.

V. CO ADSORPTION ON NiO(100)

Experimentally[26,27] it is known that CO adsorbs exothermally on NiO(100) with an adsorption energy of 0.3 eV and an adsorption bond length Ni-C of 2.07 Å. The C-O bond length remains 1.15 Å, close to the gas-phase bond length. Both the Ni-C ($\sim 7\pm 3°$) and the C-O ($12\pm 6°$) bonds are tilted with respect to the surface normal. Compared to CO adsorbed on the metallic Ni(111) surface, which has an adsorption energy of $\sim$1.2 eV, the adsorption on NiO(100) is much weaker.

Former calculations of Pacchioni *et al.*[28] and Pöhlchen and Staemmler[29] for this system performed in the Hartree-Fock approximation and using small clusters to represent the NiO surface show a substantial overestimation of the Ni-C bond length while underestimating the adsorption energy only slightly (see Table III). The tilts are not reproduced.

TABLE II. NiO surface properties: band gap $\Delta\epsilon$, surface energy γ, magnetic moment in the surface layer, m, relaxation of the distance between the first and second (Δ_{12}), and second and third layer (Δ_{23}), and height difference of the Ni and O atoms in the first layer (buckling b).

	Experiment	Theory				
		Present work				Dudarev *et al.* (Ref. 24)
		LSDA+U $U=6.3$ eV	SGGA+U $U=6.3$ eV	SGGA	LSDA	LSDA+U $U=8$ eV
$\Delta\epsilon$ (eV)		2.8	2.9	0.1	0	3.3 (bulk 3.5)
γ (meV/Å^3)		41	49	53	71	
m (μ_B)		1.62	1.71	1.21	1.07	1.72 (bulk 1.74)
Δ_{12} (%)	-2[a]	-1.3	-1.04	-1.6	$+1.4$	
Δ_{23} (%)	0	$+0.8$	$+0.50$	$+0.7$	-1.4	
b (Å)		0.023	0.017	0.015	0.1	

[a]Reference 58.

Very recently Bredow[32] used cluster-based Hartree-Fock, density-functional, and hybrid methods to investigate the adsorption of CO on NiO(100). The rather wide scatter in the Hartree-Fock results illustrate the difficulties to achieve convergence with respect to cluster size and basis set. The best agreement for the Ni-C bond length is achieved using the B3LYP hybrid functional, but it also gives an almost zero adsorption energy and a too large negative shift of the C-O stretching frequency. The possibility of a tilted adsorption geometry was evidently not considered, but we note that Di Valentin *et al.*[31] found a stable tilted geometry for NO on NiO(100) using B3LYP. All other methods lead to a substantial disagreement for the adsorption length.

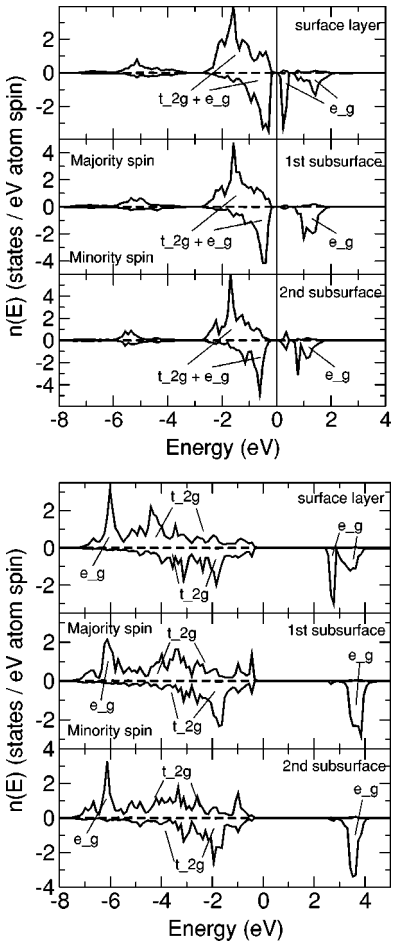

FIG. 4. Projected density of states of Ni-3d states for nickel ions of the surface, first subsurface, and second subsurface layer from (a) SGGA and (b) SGGA+U, $U=6.3$ eV.

A. Adsorption geometry and energy

We have examined the adsorption of CO on NiO(100) using the LSDA, SGGA, LSDA+U, and SGGA+U methods, with $U=6.3$ eV, as optimized for bulk NiO. The two topmost layers and the CO molecule were allowed to relax. The coverage was varied between 1 ML, 0.5 ML, and 0.25 ML (where ML stands for monolayer) by using $c(1\times1)$, $c(\sqrt{2}\times\sqrt{2})$ and $c(2\times2)$ supercells, respectively (see Fig.

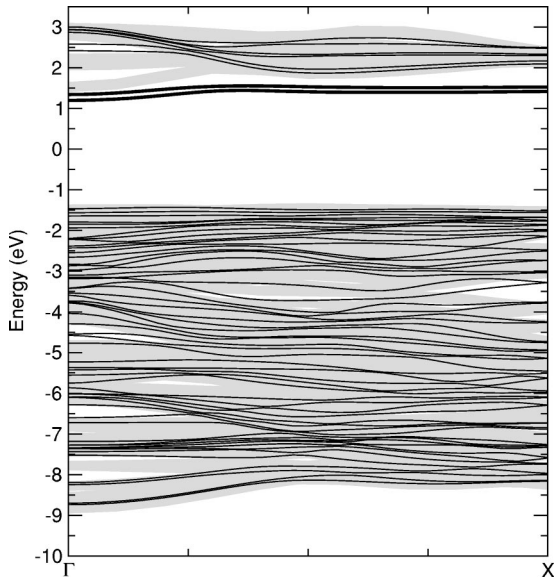

FIG. 5. Dispersion relations calculated for the slab model of NiO (full lines) and bulk density of states projected onto the surface Brillouin zone (gray shading). The electronic surface states, split from the conduction band, are clearly visible.

TABLE III. Overview of calculated adsorption properties of CO on NiO(100). The calculations were done with $\Theta = 0.25$, 0.5, and 1 ML CO coverages. LSDA, SGGA, and DFT+U were used.

	d_{Ni-C}	d_{C-O}	ϕ_{Ni-C}	ϕ_{C-O}	Adsorption energy (eV)
Experiment[a]	2.07	1.15	7°±3°	12°±6°	0.3
Theory					
HF[b]	2.49				0.25
HF[c]	2.86				0.08
HF[d]	2.92	1.105			0.00
HFLYP[d]	2.40	1.098			0.19
B3LYP[d]	2.10	1.134			0.02
BLYP[d]	1.87	1.161			0.23
Present work—Theory					
DFT					
LSDA, $\Theta = 0.5$ ML	1.76	1.150	0°	0°	1.26
SGGA, $\Theta = 0.25$ ML	1.81	1.154	0°	0°	0.73
SGGA, $\Theta = 0.5$ ML	1.81	1.153	0°	0°	0.70
SGGA, $\Theta = 1$ ML	1.82	1.153	0°	0°	0.68
DFT+U ($U = 6.3$ eV)					
LSDA+U, $\Theta = 0.25$ ML	1.93	1.144	4.5°	11.3°	0.80
LSDA+U, $\Theta = 0.5$ ML	1.94	1.145	6.6°	18.1°	0.79
LSDA+U, $\Theta = 1$ ML	1.95	1.146	7.0°	16.2°	0.77
SGGA+U, $\Theta = 0.25$ ML	2.03	1.143	5.9°	15.1°	0.33
SGGA+U, $\Theta = 0.5$ ML	2.04	1.145	7.3°	21.0°	0.26
SGGA+U, $\Theta = 1$ ML	2.05	1.146	5.6°	14.7°	0.19

[a]Hoeft *et al.*, Refs. 26 and 27.
[b]Pacchioni *et al.*, Ref. 28, cluster calculations, CO bond length fixed.
[c]Pöhlchen and Staemmler, Ref. 29, cluster calculations, CO bond length fixed.
[d]Bredow, Ref. 32, cluster calculations, coverage not defined.

6). Initially the CO molecule was kept parallel to the surface normal, but in a second step a tilt with respect the surface normal was considered. In a range of Ni-C-O angles from 0° to 30°, starting points for relaxations were defined at intervals of 5° for tilts in both the [010] and the [001] directions.

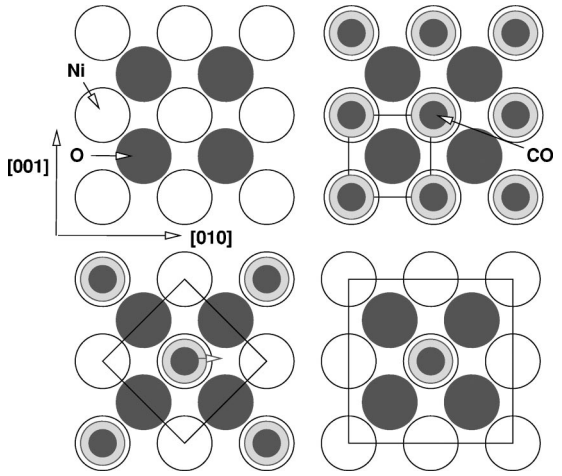

FIG. 6. The clean NiO(100) surface (upper left), the (1×1) surface cell ($\Theta_{CO} = 1$ ML), the $\sqrt{2}\times\sqrt{2}$ ($\Theta_{CO} = 0.5$ ML) (lower left), and the 2×2 ($\Theta = 0.25$ ML) supercells (lower right). The preferred tilt direction is indicated by the arrow (lower left panel).

Initially, the angles between the surface normal and the Ni-C and C-O bonds were assumed to be the same. For each of these initial configurations, the z ([001]) and y ([010]) coordinates of the O atom were fixed, so that the atom could only move in the [100] direction. The C atom was free to move in all directions so that the angles of the Ni-C and C-O bonds relative to the surface normal can be different and both the Ni-C and C-O bond lengths can be optimized. The variation of the adsorption energy as a function of the tilting angle of the C-O band is illustrated in Figs. 7 and 8, and adsorption energies, bond lengths, and tilting angles for the optimal adsorption geometry are summarized in Table III and compared with experiment and previous theoretical studies.

In both the LSDA and SGGA, any tilting of the molecule from a perpendicular position is energetically unfavorable. In the LSDA, the calculated Ni-C bond length is too short by 0.4 Å; the calculated adsorption energy is four times higher than measured. This is characteristic for the overbinding tendency of the LSDA. Generalized gradient corrections lead only to a marginal improvement: a small increase in the adsorption distance by 0.05 Å (which is still much too small) and a reduction of the adsorption energy by nearly 50% (which is still too large). For the Ni-C bond length, our SGGA results are rather close to the BLYP results of Bredow,[32] but the PW functional or the plane-wave basis set leads to a much larger adsorption energy. Only if the on-site

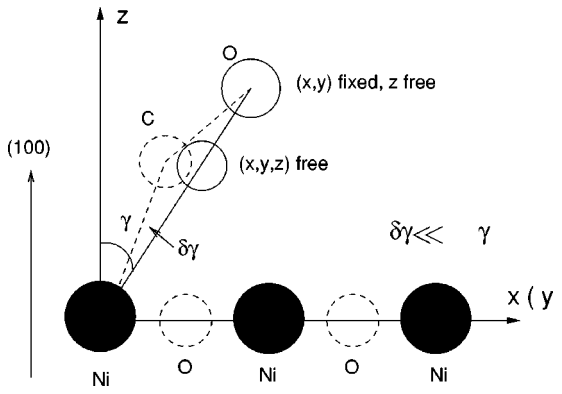

FIG. 7. Initial configuration for a relaxation of the tilted CO molecule on top of the Ni adatom at one of the predefined tilting angles. The *x* and *y* coordinates of the O molecule are kept fixed during a calculation while the *z* coordinate is free. The C molecule is free to move. The movements are very small, thus $\Delta\gamma/\gamma \ll 1$.

Coulomb repulsion is added to the DFT functional, tilting was found to be energetically stable in both [010] and [001] directions, with a tilt towards the oxygen atom ([001] direction) in the surface plane being energetically less stable than a tilt towards the nickel atom ([010] direction). The tilting is strongest at a coverage of 0.5 ML, at larger coverage lateral interactions reduce the tilting. At the lower coverage of 0.25 ML, the increasing adsorbate-substrate bonding also reduces the tendency to tilt away from the surface normal. In the LSDA+U, the Ni-C bond length is still too small by about 0.24 Å and the adsorption energy is largely overestimated. In agreement with our results on bulk NiO and on the clean surface, the best results are achieved using the SGGA+U approach: Ni-C, C-O bond lengths, tilting angles, and adsorption energies agree almost perfectly with experiment. As the results compiled in Table III demonstrate, the calculated Ni-C bond length agrees with experiment within 0.02 Å, the tilt angles also agree within the experimental uncertainty, and even the adsorption energies are accurate to within 0.05 eV.

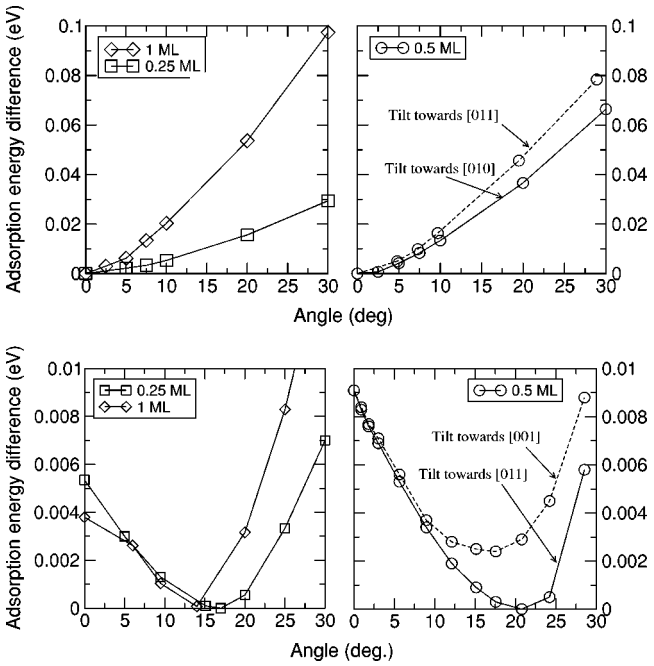

FIG. 8. Variation of the adsorption energy of CO on NiO(100) as a function of the tilting angle of the adsorbed molecule, as calculated at different coverages using (a) the SGGA and (b) the SGGA+U. For a coverage of 0.5 ML, the possibilities of a tilting towards a neighboring Ni atom (i.e., in the [011] direction) or towards a neighboring O atom ([001] direction) have been explored.

B. Bonding mechanism

The tilted adsorption geometry for a weakly adsorbed linear molecule such as CO is a rather surprising result. On the surfaces of transition metals, CO is usually adsorbed in an upright position for metals with a nearly full *d* band. On the surfaces of metals with a half or less than half-filled *d* band, CO is dissociated. Only on the relatively open α-Fe(100) surface, CO is molecularly adsorbed in a tilted configuration, forming an angle of $45\pm10°$ with respect to the surface normal[60–62] and dissociates upon heating. In contrast, both on the close-packed (110) surface of α-Fe and on the surfaces of thin films of γ-Fe, CO is adsorbed in an upright position[63] and desorbs in molecular form. Hence in these cases, the tilted configuration appears as a precursor to dissociation, and adsorbate-substrate interactions are mediated by strong covalent bonds. It has been shown[64] that the tilting observed on the α-Fe(100) surface is induced by a strong hybridization between O-*p* orbitals extending parallel to the surface and t_{2g} orbitals of the substrate atoms. However, it cannot be expected that these results, which apply to a strong-bonding situation, can be transferred straightforwardly to the weakly bonded CO on NiO.

Quite generally, the bonding of a CO molecule to a transition-metal atom of the substrate can be attributed to the hybridization of the highest occupied molecular orbital (HOMO) and the lowest unoccupied molecular orbital (LUMO) of CO with *d* orbitals in the appropriate energy range. For CO on NiO(100) this leads to the following scenario:[28] (i) The empty Ni-d_{z^2} build hybrid orbitals with the fully occupied 5σ HOMO of CO (donation), (ii) the occupied Ni-d_{zx} and Ni-d_{zy} orbitals build hybrid orbitals with the unoccupied $2\pi^*$ LUMO of CO (back-donation). The former process contributes to the formation of the adsorbate-substrate bond and the latter to the reduction of the intramolecular bond strength. The adsorption properties of CO on NiO(100) are therefore dependent on the degree of hybridization of these orbitals, which depends on their relative position.

The source of failure of the LSDA and SGGA calculations, where the Ni-C bond length is substantially underestimated and the adsorption energy is overestimated, is the incorrect description of the Ni-*d* states, leading to a too strong hybridization between the $2\pi^*$ LUMO of CO and the filled Ni-d_{zx} and Ni-d_{zy} states and to a reduction of the intramolecular bond strength. In DFT+U calculations the increased exchange splitting pushes the Ni-t_{2g} states to much lower energies and reduces strongly the $2\pi^*$-$(d_{zx}+d_{zy})$ hybridization and hence the adsorption strength.

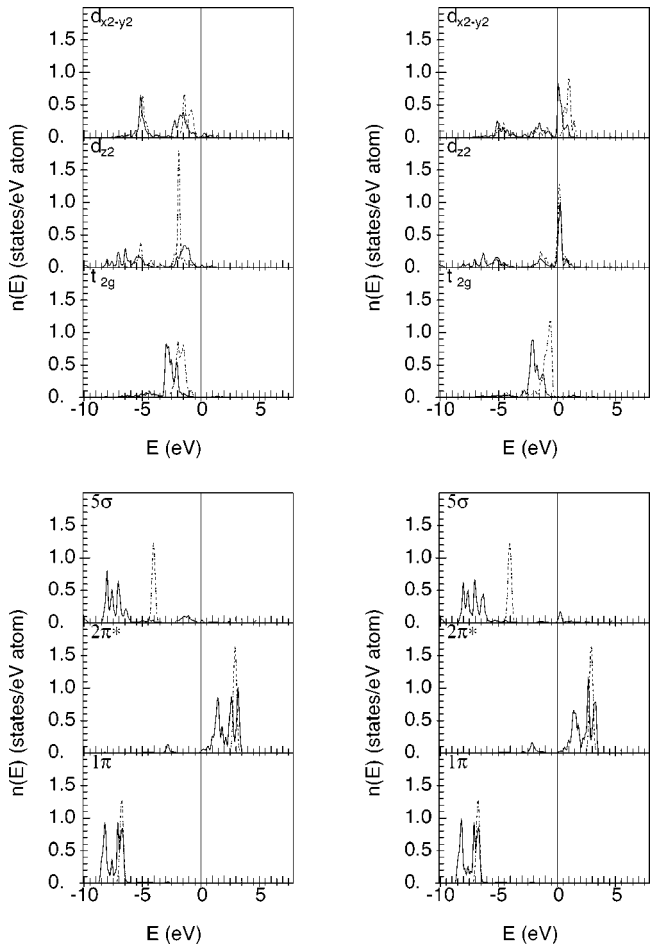

FIG. 9. SGGA calculations for CO adsorbed on NiO (coverage 0.5 ML), upright adsorption geometry: The upper panel shows Ni-3d orbitals for the clean site (dashed line) and adatom site (solid line). The lower panel shows C-2p orbitals for a CO molecule in a Ni-C distance of 3 Å (dashed line) and an adsorbed CO molecule (solid line).

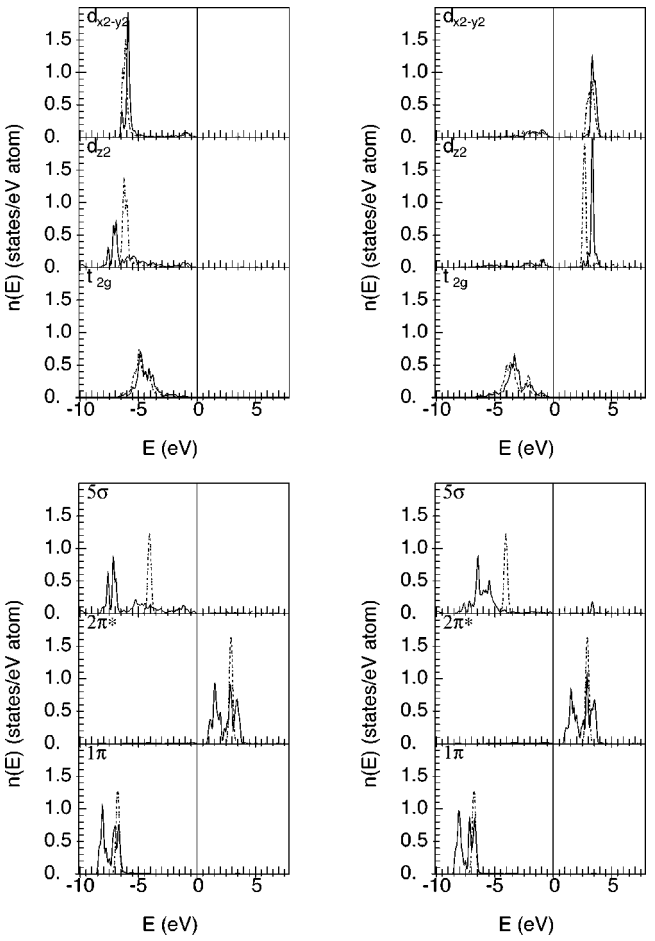

FIG. 10. SGGA+U calculations for CO adsorbed on NiO (coverage 0.5 ML), upright adsorption geometry. The upper panel shows Ni-3d orbitals for clean site (dashed line) and adatom site (solid line). The lower panel shows C-2p orbitals for a CO molecule in a Ni-C distance of 3 Å (solid line) and an adsorbed CO molecule (dashed line).

These effects are very clearly reflected in the local partial densities of states. Figures 9 and 10 compare the results for the spin-polarized Ni-t_{2g}, -d_{z^2}, and-$d_{x^2-y^2}$ states and for the $2\pi^\star$, 5σ, and 1π molecular orbitals of CO as obtained in the SGGA, without and with the on-site Coulomb repulsions. In the SGGA, the significant features are the broadening and bonding/antibonding splitting of the Ni-d_{z^2} and CO 5σ DOS's as well as the bonding/antibonding splitting in the CO $2\pi^\star$ DOS, leading to an incipient population of these antibonding molecular orbitals. In the SGGA+U, the d_{z^2}-5σ interaction is reduced to the majority states and the $2\pi^\star$ states remain completely empty. This means that mechanism (i) dominates the adsorbate-substrate bond.

While the analysis of the projected DOS helps us to understand the reduction of the adsorption strength resulting from the electronic correlation effects, the tilting of the molecule is a more subtle effect. DFT (LSDA or SGGA)+U predicts a substantial tilt of both Ni-C and C-O bonds. In the upright configurations, only the 5σ-d_{z^2} and $2\pi^*$-($d_{zx}+d_{zy}$) interactions are nonzero by symmetry. The former ($pd\sigma$)-type coupling is relatively insensitive against a tilting of the molecule, while the latter ($pd\pi$)-type coupling strongly prefers the upright configuration. If the ($pd\pi$) interaction is strong (as in LSDA and SGGA), the upright high-symmetry configuration is the stable one. In the SGGA+U calculations, this type of interaction is strongly reduced by the increased exchange splitting, as evidenced by the lack of a $2\pi^*$ peak at the energy of the t_{2g} states. Hence, the bonding between the substrate and the molecule is no longer directional, and the CO molecule can tilt without a significant loss of covalent binding energy. Furthermore, in a symmetry-broken tilted configuration, the d_{z^2} states can interact with both π orbitals of the CO molecule (initially symmetry forbidden). The corresponding changes in the local partial densities of states are found to be rather minute. To underline the previous argument we show in Fig. 11 charge-density flow (difference electron density) diagrams for CO in an upright and a tilted configuration as calculated in SGGA+U. In both figures negative charge flow (dark color) is located at the Ni-d_{zx}/Ni-d_{zy} and the CO-5σ orbitals, while positive charge flow (light gray color) is located at the Ni-d_{z^2} and the CO-$2\pi^*$ orbitals, indicating the two bonding mecha-

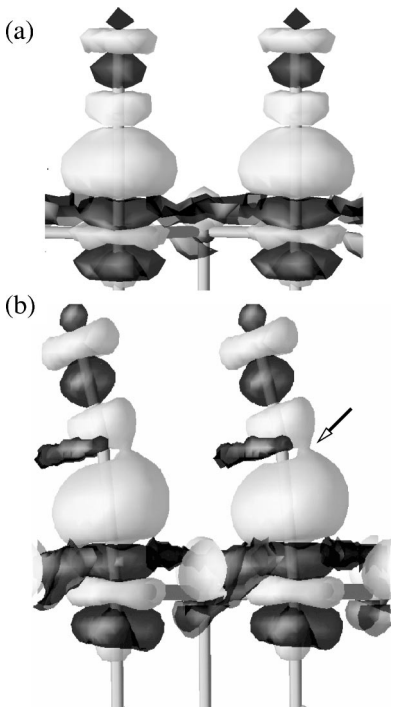

FIG. 11. Charge flow diagram (difference electron densities) as calculated in the SGGA+U for CO in the upright (top) and tilted (bottom) adsorption positions.

nisms discussed above. In the tilted configuration, an additional lobe with negative charge flow appears at the C atom pointing towards the tilting direction, and a charge accumulation is visible at the opposite side of the C atom indicated by an arrow in Fig. 11. These features are caused by the rehybridization of the 1π and $2\pi^*$ orbitals with the d_{z^2} states, resulting in a small net binding. Certainly the strength of the binding can be determined only on the basis of a full *ab initio* calculation, and it is difficult to deduce it from a simplified analysis on the basis of the density of states or charge flow.

VI. CONCLUSIONS

We have presented a comprehensive investigation of the physical properties of bulk NiO, of clean and CO-covered NiO(100) surfaces, both using density-functional theory and using the DFT+U approach in which a Hubbard term describing the strong on-site Coulomb interactions is added to the density-functional Hamiltonian. In the past repeated attempts have been made to describe the properties of the strongly correlated transition-metal oxides within the DFT framework, but it remained unclear whether a comprehensive description of all physical properties could be achieved with a single value of the on-site Coulomb potential. It should also be emphasized that various DFT variants may be found in the literature, differing in the way in which the energy contributions which are included in both the Hubbard term and in the DFT Hamiltonian are subtracted out. In our calculations we have adopted the rotationally invariant formulation of the DFT+U Hamiltonian introduced by Liechtenstein *et al.*[16] and Dudarev *et al.*[17] and implemented it in the projector-augmented-wave method, which is one of the most accurate full-potential all-electron electronic structure methods. We have also investigated both local (LSDA) and gradient-corrected (SGGA) exchange-correlation functionals.

The comparison of the LSDA+U and SGGA+U for bulk NiO leads to the first important result: while in the LSDA+U approach it turns out to be difficult to achieve good agreement for all physical properties—to fit the equilibrium volume and bulk modulus to experiment would require a substantially larger value of the on-site potential than required to fit the band gap or the magnetic moments—consistent description with a physically reasonable value of $U=6.3$ eV is achieved in the SGGA+U, which also improves the calculated binding energy. A SGGA+U calculation also leads to a good description of the clean NiO surface. The result that the Hubbard on-site term should be used best in conjunction with a gradient-corrected DFT functional confirms very recent results on the less strongly correlated transition-metal sulfides. For bulk NiO we find that the SGGA+U description leads to similar results as calculations based on hybrid functionals mixing exact exchange to the SGGA functional.[19]

We have shown that the strong on-site correlations lead to a qualitative change in the adsorption behavior of CO on NiO. While a pure DFT (LSDA or SGGA) approach predicts a strong-binding situation and an upright adsorption geometry, the SGGA calculation leads to an adsorption geometry and energy in perfect agreement with experiment. This is achieved with the same value of the on-site Coulomb potential that has been used in the bulk calculations. The weak binding and the tilting of the molecule away from the surface normal are shown to result from the increased exchange splitting of the Ni-d states, which largely suppresses the $2\pi^*$-$(d_{zx}+d_{zy})$ interaction and enables a 1π-d_{z^2} hybridization favoring the tilted geometry.

Whereas for bulk NiO the use of a hybrid B3LYP functional provides a physically reasonable interpolation between the HF approaches (which overestimate gap and exchange splitting) and DFT (leading to metallic behavior), the situation is different for CO adsorption: in this case B3LYP predicts a reasonable Ni-C bond, but an almost unbound CO molecule.

In summary, using CO on NiO surfaces as a testing ground, we have demonstrated that a DFT+U approach could provide not only a reasonable strategy for calculating not only the bulk properties of strongly correlated transition-metal compounds, but in addition lead to significant advances in the description of molecular adsorption on the surfaces of these important materials as well. Preliminary results on other TMO's and their surfaces (Fe_2O_3, Cr_2O_3, etc.)[65–67] suggest that these conclusions drawn here for a test system have more general validity.

ACKNOWLEDGMENTS

This work has been supported by the Austrian Science Funds through the Science College ''Computational Materials Science.''

[1] C. Noguera, *Physics and Chemistry of Oxide Surfaces* (Cambridge University Press, Cambridge, 1996).
[2] V. E. Henrich and P. A. Cox, *The Surface Science of Metal Oxides* (Cambridge University Press, Cambridge, 1994).
[3] P. A. Cox, *Transition Metal Oxides: An Introduction to their Electronic Structure and Properties*, The International Series of Monographs on Chemistry Vol. 27 (Clarendon Press, Oxford, 1995).
[4] A. Eichler and J. Hafner, Chem. Phys. Lett. **343**, 383 (2001).
[5] G.A. Sawatzky and J.W. Allen, Phys. Rev. Lett. **53**, 2339 (1984).
[6] B.E.F. Fender and A.I. Jacobson, J. Chem. Phys. **48**, 990 (1968).
[7] A.K. Cheetham and D.A.O. Hope, Phys. Rev. B **27**, 6964 (1983).
[8] A. Fujimori and F. Minami, Phys. Rev. B **30**, 957 (1984).
[9] S. Hüfner, J. Osterwalder, T. Riesterer, and F. Hulliger, Solid State Commun. **52**, 793 (1984).
[10] F. Aryasetiawan and O. Gunnarsson, Phys. Rev. Lett. **74**, 3221 (1995).
[11] S. Massidda, A. Continenza, M. Posternak, and A. Baldereschi, Phys. Rev. B **55**, 13 494 (1997).
[12] A. Svane and O. Gunnarsson, Phys. Rev. Lett. **65**, 1148 (1990).
[13] Z. Szotek, W.M. Temmerman, and H. Winter, Phys. Rev. B **47**, 4029 (1993).
[14] C. Calandra and F. Manghi, Phys. Rev. B **50**, 2061 (1994).
[15] V.I. Anisimov, J. Zaanen, and O.K. Andersen, Phys. Rev. B **44**, 943 (1991).
[16] A.I. Liechtenstein, V.I. Anisimov, and J. Zaanen, Phys. Rev. B **52**, R5467 (1995).
[17] S.L. Dudarev, G.A. Botton, S.Y. Savrasov, C.J. Humphreys, and A.P. Sutton, Phys. Rev. B **57**, 1505 (1998).
[18] M.D. Towler, N.L. Allan, N.M. Harrison, V.R. Saunders, W.C. Mackrodt, and E. Apra, Phys. Rev. B **50**, 5041 (1995).
[19] Th. Bredow and A.R. Gerson, Phys. Rev. B **61**, 5194 (2000).
[20] C. Lee, W. Yang, and R.G. Parr, Phys. Rev. B **37**, 785 (1988).
[21] A.D. Becke, J. Chem. Phys. **98**, 5648 (1993).
[22] A. Gorschlüter and H. Merz, Phys. Rev. B **49**, 17 293 (1994).
[23] M.R. Castell, P.L. Wincott, N.G. Condon, C. Muggelberg, G. Thornton, S.L. Dudarev, A.P. Sutton, and G.A.D. Briggs, Phys. Rev. B **55**, 7859 (1997).
[24] S.L. Dudarev, A.I. Liechtenstein, M.R. Castell, G.A.D. Briggs, and A.P. Sutton, Phys. Rev. B **56**, 4900 (1997).
[25] H. Kuhlenbeck, G. Odörfer, R. Jaeger, G. Illing, M. Menges, Th. Mull, H.J. Freund, M. Pöhlchen, V. Staemmler, S. Witzel, C. Scharfschwerdt, K. Wennemann, T. Liedtke, and M. Neumann, Phys. Rev. B **43**, 1969 (1991).
[26] J.-T. Hoeft, M. Kittel, M. Polcik, S. Bao, R.L. Toomes, J.H. Kang, D.P. Woodruff, M. Pascal, and C.L.A. Lamont, Phys. Rev. Lett. **87**, 086101 (2001).
[27] M. Kittel, J.-T. Hoeft, S. Bao, M. Polcik, R.L. Toomes, J.H. Kang, D.P. Woodruff, M. Pascal, and C-L.A. Lamont, Surf. Sci. **499**, 1 (2002).
[28] G. Pacchioni, G. Cogliandro, and P.S. Bagus, Surf. Sci. **255**, 344 (1991).
[29] M. Pöhlchen and V. Staemmler, J. Chem. Phys. **97**, 2583 (1992).
[30] T. Klüner, H.-J. Freund, V. Staemmler, and R. Kosloff, Phys. Rev. Lett. **80**, 5208 (1998).
[31] C. Di Valentin, G. Pacchioni, Th. Bredow, D. Dominguez-Ariza, and F. Illas, J. Chem. Phys. **117**, 2299 (2002).
[32] Th. Bredow, J. Phys. Chem. B **106**, 7053 (2002).
[33] G. Kresse and J. Hafner, Phys. Rev. B **47**, 558 (1993).
[34] G. Kresse and J. Hafner, Phys. Rev. B **49**, 14 251 (1994).
[35] G. Kresse and J. Furthmüller, Phys. Rev. B **54**, 11 169 (1996).
[36] G. Kresse and J. Furthmüller, Comput. Mater. Sci. **6**, 15 (1996).
[37] G. Kresse and D. Joubert, Phys. Rev. B **59**, 1758 (1999).
[38] P.E. Blöchl, Phys. Rev. B **50**, 17 953 (1994).
[39] O. Bengone, M. Alouani, P. Blöchl, and J. Hugel, Phys. Rev. B **62**, 16 392 (2000).
[40] J.P. Perdew and A. Zunger, Phys. Rev. B **23**, 5048 (1981).
[41] D.M. Ceperley and B.J. Alder, Phys. Rev. Lett. **45**, 566 (1980).
[42] J.P. Perdew, J.A. Chevary, S.H. Vosko, K.A. Jackson, M.R. Pederson, D.J. Singh, and C. Fiolhais, Phys. Rev. B **46**, 6671 (1992).
[43] S.H. Vosko, L. Wilk, and M. Nusair, Can. J. Phys. **58**, 1200 (1980).
[44] E.G. Moroni, G. Kresse, J. Hafner, and J. Furthmüller, Phys. Rev. B **56**, 15 629 (1997).
[45] A. Gross, S. Wilke, and M. Scheffler, Phys. Rev. Lett. **75**, 2718 (1995).
[46] A. Eichler, J. Hafner, A. Gross, and M. Scheffler, Phys. Rev. B **59**, 13 297 (1999).
[47] D.M. Wood and A. Zunger, J. Phys. A **18**, 1343 (1985).
[48] D.D. Johnson, Phys. Rev. B **38**, 12 807 (1988).
[49] P. Pulay, Chem. Phys. Lett. **73**, 393 (1980).
[50] H.J. Monkhorst and J.D. Pack, Phys. Rev. B **13**, 5188 (1976).
[51] O. Jepsen and O.K. Anderson, Solid State Commun. **9**, 1763 (1971).
[52] M. Methfessel and A.T. Paxton, Phys. Rev. B **40**, 3616 (1989).
[53] P.E. Blöchl, O. Jepsen, and O.K. Andersen, Phys. Rev. B **49**, 16 223 (1994).
[54] J. van Elp, H. Eskes, P. Kuiper, and G.A. Sawatzky, Phys. Rev. B **45**, 1612 (1992).
[55] N. Wassdahl, P. Bleckert, G. Bray, P. Glans, N. Martensson, J. Nordgren, J.E. Rubensson, R. Nyholm, and S. Cramm, in *X-Ray and Inner-Shell Processes*, edited by T.A. Carlson, M.O. Krause, and S.T. Manson, AIP Conf. Proc. No. 215 (AIP, New York, 1990), p. 451; as cited by Ref. 56.
[56] V.I. Anisimov, P. Kuiper, and J. Nordgren, Phys. Rev. B **50**, 8257 (1994).
[57] Z.X. Shen, R.S. List, D.S. Dessau, B.O. Wells, O. Jepsen, A.J. Arko, R. Barttlet, C.K. Shih, F. Parmigiani, J.C. Huang, and P.A.P. Lindberg, Phys. Rev. B **44**, 3604 (1991).
[58] M.R. Castell, S.L. Dudarev, G.A.D. Briggs, and A.P. Sutton, Phys. Rev. B **59**, 7342 (1999).
[59] F.P. Netzer and M. Prutton, J. Phys. C **8**, 2401 (1975); M.R. Welton-Cook and M. Prutton, *ibid.* **13**, 3993 (1980).
[60] D.W. Moon, D.J. Dwyer, and S.L. Bernasek, Surf. Sci. **163**, 215 (1985).
[61] D.W. Moon, S.L. Bernasek, J.P. Lu, J.L. Galnd, and D.J. Dwyer, Surf. Sci. **184**, 90 (1987).
[62] J.P. Lu, M.R. Albert, C.C. Chanmg, and S.L. Bernasek, Surf. Sci. **227**, 317 (1990).
[63] J. Radnik, E. Chopovskaya, M. Grüne, and K. Wandelt, Surf. Sci. **352-354**, 268 (1996).
[64] A. Stibor, G. Kresse, and J. Hafner (unpublished).
[65] A. Rohrbach, J. Hafner, and G. Kresse, J. Phys.: Condens. Matter **15**, 979 (2003).
[66] G. Rollmann, A. Rohrbach, P. Entel, and J. Hafner, Phys. Rev. B (to be published).
[67] A. Rohrbach, G. Kresse, and J. Hafner (unpublished).